

Postprint: High-Temperature Vacuum Carburizing Behavior and Phase Evolution Mechanism of In-Service Cr₃₅Ni₄₅Nb Alloy

Authors: Peng Yichao, Zhang Maicang, Du Chenyang, Dong Jianxin

Date: 2023-03-19T00:00:00+00:00

Abstract

Accelerated carburization treatment was performed on the Cr₃₅Ni₄₅Nb alloy of ethylene cracking furnace tubes that had been in service for 6 years using acetylene vacuum carburization, and systematic investigations on the carburization behavior and phase evolution mechanism of the furnace tube inner wall before and after carburization were conducted using SEM, XRD, and quantitative electron probe microanalysis. The results indicate that a relatively thick Cr₂O₃/SiO₂ composite oxide layer formed on the inner surface of the furnace tubes. The composite oxide layer exhibited excellent corrosion resistance and served as an effective barrier preventing carbon infiltration into the furnace tube interior. The anti-carburization capability of the material primarily depends on the continuity and density of the surface Cr₂O₃ layer and the stability of the subsurface SiO₂ layer. In atmospheres with low oxygen partial pressure and reducing characteristics, the surface Cr₂O₃ layer gradually carbonizes to Cr₃C₂, and the Cr₃C₂ progressively spalls and peels off, causing the anti-carburization capability of the protective Cr₂O₃ film to gradually weaken and even disappear. Although the subsurface SiO₂ possesses excellent thermodynamic stability, the low activity of Si results in a discontinuous SiO₂ layer, allowing partial carbon infiltration through the voids in the oxide layer. When this composite oxide layer is removed or the carburization time is sufficiently long such that the anti-carburization capability of the composite oxide layer deteriorates sharply, significant microstructural changes occur within the furnace tube material due to severe internal carburization: interdendritic carbides severely coalesce and coarsen, and undergo in-situ transformation from M₂₃C₆ to M₇C₃, while a vermicular γ phase similar to divorced eutectoid morphology precipitates within the carbides. The closer to the surface, the higher the carbon activity, resulting in metal dusting characterized by massive graphite precipitation within a depth of approximately 0.5 mm. Severe coalescence and coarsening of carbides, along

with metal dusting phenomena, cause severe weakening of the furnace tube microstructure, generation of macrocracks, and reduction in furnace tube service life.

Full Text

Preamble

Vol. 51, No. 1, January 2015, pp. 11-20

ACTA METALLURGICA SINICA

High Temperature Vacuum Carburization Behaviors and Phase Evolution Mechanisms of Cr35Ni45Nb Alloy Under Service Condition

PENG Yichao¹, ZHANG Maicang¹, DU Chenyang², DONG Jianxin¹

¹ School of Materials Science and Engineering, University of Science and Technology Beijing, Beijing 100083

² China Special Equipment Inspection and Research Institute, Beijing 100013

ABSTRACT: Carburization in Ni-Cr-Fe-based alloys is an important phenomenon, especially in ethylene cracking tubes which serve at high temperatures under highly carburizing environment. In this work, the Cr35Ni45Nb tube subjected to service condition for 6 a was carburized by low-pressure vacuum carburizing (LPVC) at 1080 °C. The carburization behaviors and corresponding mechanisms of phase evolution in the inner wall were comprehensively analyzed through SEM, XRD and EPMA. The results showed that oxidation behaviors of the tube at high temperature consisted of external oxidation of Cr and internal oxidation of Si, resulting in formation of composite oxide scales. Depletion of Cr in the subsurface caused by surface Cr₂O₃ led to carbide dissolution and formation of carbide free zone and carburized zone. The critical concentration of Cr for carbide dissolution is about 19.0% (mass fraction). By comparing carburization behaviors of specimens whose oxide scales were retained or removed, the carburization resistance of the composite oxide scales in carburizing environment was systematically investigated. The results showed that the composite oxide scales formed previously acted as an effective barrier to carbon infiltration. However, the outermost Cr₂O₃ scale tended to be carbonized to form carbide scale to spall from the surface in the strongly reducing environment with low oxygen partial pressure, while the SiO₂ kept stable all along due to its excellent thermodynamic stability. However, a certain amount of carbon was still capable of penetrating the alloy interior through gaps of the SiO₂ scale due to its discontinuity. Therefore, continuity, density and high-temperature stability of the oxide scales were crucial for the alloy to achieve excellent anti-carburizing performance. Once the oxide layers were removed or carbonized adequately, inconceivable internal carburization occurred widely. Large amounts of secondary carbides precipitated again in the previous carbide free zone due to high carbon activity. Widespread precipitations of graphite called metal dusting in the range of about 0.5 mm in depth occurred after long exposure of specimens

to the carburizing environment. The carbon activity gradually decreased with increasing distance from the surface. The primary carbides within the deeper carburized region were transformed from $M_{23}C_6$ to M_7C_3 in situ, which were accompanied by precipitation of vermicular γ -phase in the primary carbides, phase transition from γ to NbC and decomposition of intragranular secondary carbides. Severe coalescing and coarsening of carbides and metal dusting caused the serious degradation of microstructure, formation of macro-cracks and final thinning of the Cr35Ni45Nb tube wall.

KEY WORDS: Cr35Ni45Nb alloy, low-pressure vacuum carburizing, anti-carburizing, oxide scale, metal dusting

Introduction

Ethylene cracking furnaces are critical equipment in the petrochemical industry for ethylene production, and the radiant section tubes represent key components whose failure can lead to unplanned shutdowns, explosions, or even more severe consequences. During service, the tube interior contains a high-velocity mixture of steam and hydrocarbons, creating a strongly carburizing and mildly oxidizing environment. Although the oxygen partial pressure inside the tubes is low, it is sufficient to oxidize Cr and Si elements, forming an oxide film on the inner wall that provides some oxidation and carburization resistance. However, numerous in-service tubes still fail due to severe carburization corrosion, primarily caused by oxide film degradation from temperature fluctuations, stress, creep, and decoking operations. Because of carbon's high diffusivity, carburization causes carbide coalescence and coarsening, significantly altering the alloy's internal microstructure and chemical composition. Under high carbon activity, severe carburization can even lead to catastrophic metal dusting of the tubes. The microstructural degradation caused by oxidation and carburization results in effective wall thickness reduction and decreased creep rupture life. While numerous studies have investigated the high-temperature oxidation behavior of tube materials under long-term service conditions, research on carburization and anti-carburization behavior during high-temperature service remains relatively limited.

This work systematically investigated the carburization behavior of a Cr35Ni45Nb heat-resistant alloy tube after 6 years of service through high-temperature low-pressure accelerated carburization experiments. The study examined carburization kinetics, the anti-carburization characteristics of composite oxide layers and their influence on carburization behavior, microstructural and phase evolution after carburization, and more severe metal dusting phenomena. The objective was to explore the carburization mechanism and oxidation-carburization superposition mechanism of this alloy under high-temperature service conditions, thereby providing a foundation for improving anti-carburization performance, establishing replacement criteria, and further

evaluating service life.

Experimental

The experimental material was a Cr35Ni45Nb radiant section tube that had been in service for 6 years (approximately 52,000 hours), with a nominal chemical composition (mass fraction, %) of: C 0.5, Nb 1.0, Cr 35.44, Ni 43.57, Ti 0.01, Si 1.6, Fe balance. Six 20 mm-high ring-shaped specimens were cut from the service-exposed tube for microstructural analysis. The inner walls of half the specimens were ground to a bright surface, while the other half remained in the as-service condition. Additionally, to study carburization kinetics, eighteen rectangular specimens measuring 20 mm × 10 mm × 5 mm were cut from the tube interior, with all surfaces initially free of oxide scale. Half of these rectangular specimens underwent a 90 h pre-oxidation treatment in an SRJX-4-13 box furnace to develop a surface oxide film. All rectangular specimens were then ultrasonically cleaned in acetone, dried, and weighed using a Sartorius-BS223S electronic balance to obtain initial masses. The specimens were divided into three batches and subjected to low-pressure vacuum carburizing in a dual-chamber vacuum carburizing furnace at 1080 °C for 1, 3, and 5 h, respectively. After carburization, the rectangular specimens were reweighed to obtain kinetic curves. To evaluate anti-carburization capability through comparison of kinetic curve trends, samples were also taken from as-cast tubes and tubes that had served for 1.5 and 2.5 years for carburization treatment.

After carburization, the ring-shaped specimens were sectioned, mechanically ground, polished, and electrolytically etched. The microstructural evolution of the surface oxide layers and internal carburized regions was analyzed using a DMAX-RB rotating anode X-ray diffractometer (XRD), JSM-6510A scanning electron microscope (SEM), JED-2300 energy dispersive spectrometer (EDS), and JXA-8230 electron probe microanalyzer (EPMA).

Results

2.1 Microstructural Characteristics of the Inner Wall in Service Condition

Figure 1a [Figure 1: see original paper] shows the microstructure of the inner wall of the Cr35Ni45Nb heat-resistant alloy tube after 6 years of service. The inner wall can be divided into three distinct regions: a surface composite oxide scale zone, a subsurface carbide-free zone, and an internal carburized zone. Figure 1b illustrates the distribution of the surface composite oxide scale, while Figures 1c-f show the corresponding elemental mappings of Ni, O, Si, and Cr, respectively. Table 1 lists the EPMA quantitative analysis results for various positions in Figure 1b. Based on the elemental mappings and EPMA analysis, the gray phase in the outer layer is Cr₂O₃, while the black phase beneath it is SiO₂. Below the SiO₂ layer lies the carbide-free zone, with the entire oxide scale thickness being approximately 80 μm. Starting from the end of the

depletion zone, SiO_2 continues to extend inward along grain boundaries as intergranular oxidation to an average depth of about 62 μm . The carbide-free zone width is approximately 230 μm , with the intergranular oxidation region being narrower than the carbide-free region. Bennett and Price proposed a “crack corrosion” mechanism to explain intergranular oxidation and internal carburization in HK40 alloy, where the intergranular oxidation zone endpoint coincides with the internal carburization zone start point. However, this study shows that the intergranular oxidation zone is much narrower than the carbide-free zone because the high Cr content in the Cr35Ni45Nb alloy matrix ensures the surface oxide scale’s density and continuity, thereby reducing O and C penetration from the environment.

Figure 2 shows the concentration profiles (with measurement errors) of various elements in the carbide-free zone of the 6-year service tube. Although each measurement point covers a limited area, Figure 2 cannot theoretically represent the complete linear distribution of elemental concentrations across the entire depletion zone. Nevertheless, the basic trends and key concentrations in Figure 2 still provide practical value. During oxide scale formation, Cr from the subsurface matrix diffuses to the surface to react with O, forming the oxide film. This leads to decreased Cr content in the region (Figure 2a) and increased critical C concentration for carbide formation, causing carbide dissolution. The Cr concentration is lowest near the surface oxide film at approximately 15.6% (mass fraction), while the Cr content at the end of the carbide-free zone is about 19.0%, indicating that 19.0% represents the critical concentration for carbide precipitation/dissolution in the carbide-free zone of Cr35Ni45Nb alloy. When Cr concentration exceeds this value, carbides can stably exist without dissolution, leading to formation of the internal carbide-enriched zone. This concentration corresponds to the critical value under low carbon activity and does not apply to carbide precipitation or dissolution under high carbon activity. Figure 2a also shows a slight increase in Ni content in the carbide-free zone, resulting from the relative decrease in Cr content. The reduced Cr content increases carbon activity in this region, causing an uphill diffusion trend for inward carbon distribution (Figure 2b).

2.2.1 Carburization Kinetics

Figure 3 [Figure 3: see original paper] shows the vacuum carburization kinetic curves for Cr35Ni45Nb tubes with different service times at 1080 °C. The mass gain curves follow similar patterns for tubes in different conditions. Without surface oxide films, the carburization mass gain curves for tubes with service times between 0–2.5 years show little difference, demonstrating that high Ni-Cr materials maintain good anti-carburization performance even after 2.5 years of service. However, the carburization mass gain of the 6-year service tube is significantly higher than other service states, indicating that its inherent anti-carburization capability has substantially degraded after 6 years of service, making it highly susceptible to carburization attack. When a pre-formed oxide film is present,

the kinetic curve shows significant deviation: the mass gain increases extremely slowly during the initial 1 h, after which the slope increases dramatically to match that of the oxide-free condition.

2.2.2 Microstructural Characteristics of the Inner Wall After Carburization

Figure 4 [Figure 4: see original paper] shows the cross-sectional microstructures of the inner wall of the 6-year service Cr35Ni45Nb tube after vacuum carburization. Significant microstructural changes occurred before and after carburization. For specimens retaining the oxide film, the surface Cr_2O_3 layer gradually carbonized due to the high surface carbon activity during vacuum carburization. Combined with the XRD pattern in Figure 5a [Figure 5: see original paper] and EPMA analysis in Table 1, this carbide is identified as M_3C_2 . However, the SiO_2 layer remained unchanged even after 5 h of carburization, demonstrating its exceptional stability relative to Cr_2O_3 in the 1080 °C vacuum carburization environment. Because the Cr_2O_3 layer was continuous and relatively thick, and the SiO_2 layer was dense with few pores and microchannels, and because carbon has no measurable solubility in the oxide layer, the composite oxide scale provided excellent anti-carburization capability. After 1 h of vacuum carburization, almost no internal carburization occurred (Figure 4a), the carbide-free zone remained without carbide precipitation, and only thin carbides precipitated at grain boundaries in the intergranular oxidation front where cracks existed.

Figure 4b shows the microstructure after 5 h of carburization without removing the oxide layer. The surface Cr_2O_3 layer has almost completely carbonized in situ, losing its anti-carburization capability. Due to volume expansion and weakened bonding with the SiO_2 layer or alloy matrix, the carbide layer experienced substantial spallation (Figure 4b). Under continued high-temperature carburization, carbon could rapidly penetrate inward through incomplete gaps in the SiO_2 layer, generating numerous carbides along grain boundaries in the depletion zone. Because the carbon flux via bulk diffusion was limited, the intragranular carbides exhibited morphologies of parallel lamellar carbides spanning grains (resembling twin boundaries) and needle-like carbides at specific angles, showing certain orientation relationships with the austenite matrix. Combined with the XRD pattern in Figure 5b and EPMA analysis in Table 1, these carbides are identified as M_7C_3 . Additionally, compared with Figure 4a, the number of internal black patches caused by graphitization gradually increased. The XRD patterns in Figure 5 also reveal that after 1 h of vacuum carburization, the graphite peaks were very weak and essentially masked by the background, whereas after 5 h, increased graphitization made the graphite peaks more pronounced.

Figure 4c shows the microstructure after 1 h of carburization with the inner wall Cr_2O_3 and partial SiO_2 oxide film removed. With the effective oxide barrier reduced, carbon could penetrate inward in large quantities via grain boundary and bulk diffusion, reaching a carburization depth of approximately 220 μm . The

typical carbide morphology features twin-like carbides and groups of granular carbides. Due to the larger bulk diffusion carbon flux compared with Figure 4b, the intragranular carbide groups were finer and more uniformly distributed.

Figure 4d shows the microstructure after 5 h of carburization with the oxide film removed. Without the anti-carburization effect of the oxide film and with extended carburization time, severe internal carburization occurred, with graphitization phenomena prevalent within a depth range of about 510 μm . Figure 6 [Figure 6: see original paper] shows the microstructural morphologies at different depths resulting from internal graphitization. EPMA analysis of various positions in the graphitization region shown in Figure 6a (Table 1) indicates that position 6 corresponds to graphite with inclusions, position 7 to M_3C_2 , position 8 to Cr_2O_3 formed in the original internal oxidation zone, and position 9 to the γ matrix. Using Thermo-Calc software, the solubility curves of carbides in the γ matrix at 1080 $^\circ\text{C}$ were calculated as shown in Figure 7 [Figure 7: see original paper]. Based on the composition at position 9 (Cr atomic fraction 6.40%, mass fraction 6.39%), the saturated carbon concentration in the γ matrix is 0.95%, while the actual measured carbon atomic fraction at position 9 is 4.10% (mass fraction 0.947%), indicating that the carbon concentration in the γ matrix around the carbides is essentially saturated.

Below the graphitization region, primary carbides M_{23}C_6 gradually transformed to M_7C_3 over a certain range, accompanied by formation of vermicular γ -phase, as shown in Figure 6b. Positions 10, 11, and 12 in Figures 6b and 6c correspond to the γ matrix, NbC, and δ -phase, respectively. This reveals that although the original NbC slowly evolved into δ -phase ($\text{Nb}_3\text{Ni}_2\text{Si}$) during the 6-year service period, in the severely carburized region under 1080 $^\circ\text{C}$ and high carbon activity, the δ -phase transformed back into white dispersed NbC particles, while Nb remained as blocky δ -phase in the tube center (Figure 6c). No secondary carbides precipitated in the γ matrix below the graphitization region. EPMA analysis of position 10 in Figure 6b (Table 1) shows that the carbon activity in this region has significantly decreased, with a Cr atomic fraction of 14.01% (mass fraction 13.58%). Based on the previous analysis of carbide-free zone formation, this Cr content is below the critical mass concentration of 19.0% for carbide stability, preventing secondary carbide precipitation and resulting in the unique microstructural characteristics of interdendritic carbide transformation/coarsening and intragranular carbide depletion.

Discussion

3.1 Analysis of the Acetylene Vacuum Carburization Process

The high-temperature carburization process involves three independent kinetic processes: (1) carbon transfer from acetylene gas to the tube surface, forming carbon-containing complexes; (2) carbon diffusion from the alloy surface into the interior; and (3) carbon reaction with carbide-forming elements (Cr, Fe) to form carbides within the alloy. The vacuum carburization process in acetylene

at high temperature has distinct characteristics. Figure 8 [Figure 8: see original paper] shows the carbon concentration profiles inside the tube wall at the end of different carburizing stages. Due to the periodic alternation between active (carburizing) and passive (diffusion) stages in the process, carbon penetrates the alloy in a “cyclic wave-like” manner. The surface carbon concentration reaches its maximum during the active stage, forming a thin carbide layer. During the passive stage, as acetylene supply stops, some surface carbide particles gradually dissolve and diffuse inward, reducing surface carbon concentration and flattening the carbide distribution profile. When the active stage resumes, the surface becomes saturated again. This cyclic repetition leads to formation of the final carburized region.

Acetylene decomposes under catalysis by Fe and Ni: $C_2H_2 \rightarrow 2C + H_2$. The mass gain per unit area after carburization is given by [?]:

$$W = \frac{A\sqrt{D_C t}}{k_2\gamma^2 P_{H_2}} \left[\left(k\gamma\sqrt{\frac{t}{D_C}} + \frac{1}{\sqrt{\pi}} \right) \exp\left(\frac{k^2\gamma^2 t}{D_C}\right) \operatorname{erfc}\left(k\gamma\sqrt{\frac{t}{D_C}}\right) - \frac{1}{\sqrt{\pi}} \right]$$

where A is the total surface area, D_C is the carbon diffusion coefficient in the alloy, k is the reaction rate constant, γ is the carbon activity coefficient, a_e is the equilibrium carbon activity at the alloy surface, t is carburization time, k_2 is the reverse reaction constant for reaction (1), P_{H_2} is hydrogen pressure, and depends on the key controlling factor of the dominant reaction process, with $\operatorname{erfc}(x)$ being the complementary error function ($\operatorname{erfc}(\infty) = 0$).

Based on the alloy surface condition, if the oxide layer is removed, there is no barrier at the gas-solid interface and the transfer rate is very fast, making diffusion the controlling factor. Equation (2) can be simplified to:

$$W/A = 2\gamma a_e \sqrt{D_C t/\pi}$$

indicating a parabolic relationship between carburization rate and time, consistent with the kinetic curves measured for rectangular specimens without oxide films in Figure 3. If a surface oxide layer exists, the surface reaction rate becomes the main controlling factor:

$$W/A = \frac{k\gamma a_e t}{k_2\gamma^2 P_{H_2}}$$

When measuring the carburization kinetic curve for specimens with surface oxide films as shown in Figure 3, the pre-formed oxide film is primarily Cr_2O_3 , while SiO_2 remains as dispersed particles with negligible anti-carburization capability. Analysis of the kinetic curve with oxide film in Figure 3 reveals that during the initial 1 h, the anti-carburization effect of the oxide film makes the

surface reaction the dominant factor affecting carburization rate, resulting in low-slope proportional relationship between mass gain and time under the same a_e. This is partly because the oxide film blocks carbon infiltration, making the carbon flux extremely small, and partly because the surface reaction reduces oxygen atoms in the oxide film. Since oxygen's relative atomic mass is greater than carbon, the transformation of surface Cr₂O₃ to Cr₃C₂ during the surface reaction causes actual weight loss in the oxide film portion, reducing overall mass gain. The carburization degree is similar to that shown in Figure 4a. After 1 h, as the oxide film gradually carbonizes completely and spalls, the surface carburization barrier disappears, and the dominant factor transitions from surface reaction back to internal diffusion, causing the slope of the kinetic curve with oxide film to rapidly increase to match the oxide-free condition.

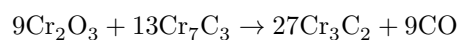
3.2 Mechanism of Oxide Layer Influence on Anti-Carburization Capability

Carbon has no measurable solubility in Cr₂O₃ oxide scales, so carbon cannot penetrate dense oxide films. However, oxide films cannot maintain perfect continuity and density during service. The formation mechanisms for pores and microchannels in oxide layers include: (1) oxide scale decomposition, particularly at grain boundaries, occurring at very low decomposition pressures applicable to the low-pressure diffusion stage; (2) cracking due to growth stresses during oxide scale thickening, applicable when the oxide layer is relatively thick; and (3) imperfect junctions between growing grains, applicable to the Cr₂O₃ layer in this study. Additionally, high-temperature creep-induced tension in the oxide layer, bonding tension between the oxide layer and substrate, thermal shock during decoking, and thermal stress can all create various defects in the surface oxide film. Through-thickness defects can serve as diffusion pathways for carbon-containing molecules, allowing carbon penetration.

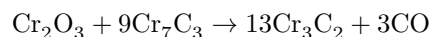
In this study, carbon penetration in the oxide layer occurs not only through defects but also through carbide formation of the oxide layer itself. In high-temperature, low oxygen partial pressure, reducing acetylene atmosphere, the surface Cr₂O₃ oxide layer is unstable and gradually carbonizes under high carbon activity, leading to progressive degradation of its anti-carburization capability. Only Cr₃C₂ and Cr₇C₃ were found in the carburized region (Figure 5 and Table 1). The oxide carbide formation process can be expressed as:



Under high carbon potential, Cr₃C₂ is more stable than Cr₇C₃ and Cr₂₃C₆, forming as the primary reaction product. If the carbon potential decreases with reaction depth within the oxide layer, the following reaction may also occur:



or alternatively:



resulting in Cr_7C_3 formation, though Cr_3C_2 remains the main reaction product. In fact, the defect-diffusion and oxide-carbide mechanisms are mutually reinforcing: numerous oxide layer pores and microchannels enable the carbonaceous atmosphere to penetrate deep into the oxide layer for decomposition and reaction with oxide particles, accelerating oxide reduction, while the resulting carbide particles further increase and expand internal defects.

Figure 9 [Figure 9: see original paper] shows the surface and cross-sectional morphologies of carbide layer spallation after surface oxide carbide formation. When carburization time is sufficient for most surface Cr_2O_3 to transform into carbide, the bonding state between the carbide layer and subsurface changes significantly. The carbide layer's low thermal expansion coefficient makes it unable to withstand the tensile stresses originally present in the oxide layer, causing extensive spallation. Once Cr_2O_3 completely carbonizes, its anti-carburization capability gradually diminishes to a minimum. Notably, this study employed accelerated carburization experiments in a high-temperature, high-carbon-potential environment; actual service temperatures and carbon potentials are much lower, significantly extending the oxide carbide formation kinetics.

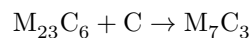
In contrast to the outer Cr_2O_3 layer, the subsurface SiO_2 layer demonstrates excellent stability, remaining almost unchanged even after 5 h of carburization, thus providing continued anti-carburization protection. SiO_2 does not reduce because SiC has far inferior thermodynamic stability compared to Cr_3C_2 and Cr_7C_3 , allowing SiO_2 to remain stable even at extremely low oxygen partial pressure (approaching zero) in the highly reducing C_2H_2 atmosphere, preventing SiC formation. Temperature is thus the determining factor for its high-temperature stability. The density of SiO_2 and carbon's extremely low solubility give it outstanding anti-carburization capability. However, because the alloy's Si content is below the critical concentration for forming a continuous SiO_2 film, Wagner's theory [?] predicts that SiO_2 particles cannot grow laterally to connect with each other, making the SiO_2 oxide layer discontinuous and allowing carbon penetration through gaps, thereby limiting anti-carburization performance.

In summary, the anti-carburization capability of the composite oxide scale results from the coordinated action of the Cr_2O_3 and SiO_2 layers, maximizing carbon infiltration resistance. Continuity, density, and high-temperature stability are three crucial factors determining oxide scale anti-carburization performance, and all are indispensable. The implications for actual tube applications include: (1) rationally adjusting alloy contents of Si, Al and other elements without compromising mechanical properties to ensure the surface composite oxide scale has good continuity, density, and high-temperature stability; and (2) ensuring that oxide scale damage and reconstruction during decoking allows the oxide

film to fully recover to a continuous, dense optimal state before cracking gas is reintroduced.

3.3 Carbide Transformation Rules

After removing the surface oxide film, the 6-year service tube's anti-carburization capability was severely weakened. Figure 3 shows that after 5 h of carburization under the same conditions, the mass gain reached 4.714 mg/cm^2 , 57.1% higher than that of the 1.5-year service tube. Before carburization, the primary carbides in the 6-year service tube had already severely coalesced and coarsened to widths of 4-9 μm ; after carburization, carbide widths increased to 20-40 μm , reaching up to 80 μm at maximum. The rapid carbide width expansion caused Cr in the matrix near carbides to diffuse rapidly toward the carbides, drastically reducing matrix Cr content and causing severe sensitization to intergranular corrosion. In non-graphitizing carburized regions, the carbide transformation can be expressed as:



In the service tube material before carburization, carbon activity is low and primary interdendritic carbides stably exist as M_{23}C_6 . After carburization, increased carbon activity in the carburized region causes primary carbides to gradually transform from M_{23}C_6 to M_7C_3 . Figures 10a [Figure 10: see original paper] and 10b show the morphology and schematic of this carbide transformation. Morphologically, this transformation resembles divorced eutectic structure, but as a solid-solid transformation, it can be considered a divorced eutectoid structure. This transformation causes some atoms originally dissolved in M_{23}C_6 to exsolve, with some entering the surrounding γ matrix and others, due to kinetic limitations, being unable to rapidly diffuse to the carbide- γ interface, forming vermicular γ -phase within the carbides. Figure 10c shows the EDS spectrum of the vermicular γ -phase. The numerous lattice defects in primary carbides provide nucleation sites for vermicular γ -phase formation. The morphology of vermicular γ -phase in M_7C_3 coarsens, elongates, and interconnects with decreasing distance from the surface (i.e., increasing carbon activity), facilitating crack propagation through dendrite arms during service.

With decreasing distance from the surface and increasing carbon activity, the coarsened primary carbides contain interconnected vermicular γ -phase with numerous gaps. The continuous carburizing atmosphere can penetrate the alloy interior through channels in the vermicular γ -phase, and the supersaturated carbon deposits as graphite within the vermicular γ -phase. This is a metal dusting phenomenon, and the high carbon activity and low oxygen partial pressure of the vacuum carburization environment provide favorable conditions for metal dusting.

Two mechanisms are proposed for severe metal dusting in the 6-year service tube after oxide film removal: (1) The Cr content in the matrix around primary car-

bides has decreased to about 6.4%, insufficient for continued chromium carbide formation, so large amounts of acetylene decompose to form graphite within the vermicular γ -phase catalyzed by Fe and Ni; and (2) Acetylene decomposition under metal catalysis produces carbon that is immediately absorbed by the metal matrix, forming stable and unstable carbides. The unstable carbides decompose under certain conditions to form metal particles and carbon, causing metal disintegration and graphite deposition. Due to the large density differences between graphite, carbides, and the matrix, extensive graphite and carbide precipitation and severe coarsening at grain boundaries cause entire grains to lift and generate macro-cracks (Figure 11 [Figure 11: see original paper]), ultimately leading to tube wall thinning and continued metal dusting penetration. Metal dusting occurrence requires that during the 6-year service period, Cr in the matrix near the tube wall was extensively consumed by intergranular oxidation or internal carburization, weakening anti-carburization capability and promoting intergranular corrosion. The surface oxide layer effectively delays or suppresses metal dusting. If the oxide film is not removed before carburization, metal dusting requires an incubation period involving oxide film carbide formation, cracking, and internal carbide development.

In non-carburized regions of the tube interior, the eutectic NbC in the original as-cast tube gradually absorbs Ni and Si atoms while expelling C atoms during long-term high-temperature aging, transforming into δ -phase with stoichiometry $\text{Nb}_3\text{Ni}_2\text{Si}$ (Figure 6c). Although NbC is relatively stable at 1080 °C, the large temperature drop inside the tube during endothermic ethylene cracking (with temperature differences up to 200 °C between inner and outer walls) means the actual service temperature is significantly lower than the nominal 1080 °C. This temperature gradient makes much of the NbC unstable, accelerating its transformation to niobium-nickel silicide. After 1080 °C vacuum carburization, δ -phase in the carburized region transforms back to NbC, indicating that δ -phase is unstable at 1080 °C under high carbon activity. Temperature is the prerequisite for this transformation, while high carbon activity is an important accelerating condition, because Nb is a strong carbide-forming element and high carbon activity shifts the NbC- δ phase transformation equilibrium leftward.

Conclusions

1. When a composite oxide scale is present, it acts as an effective barrier to carbon infiltration. The anti-carburization capability depends on the continuity, density, and high-temperature stability of the oxide film. The composite oxide scale's anti-carburization performance results from the coordination between the Cr_2O_3 layer's good continuity, density, and thickness, and the SiO_2 layer's excellent density and stability, maximizing carbon infiltration resistance.
2. In low oxygen partial pressure, reducing acetylene atmosphere, the surface Cr_2O_3 layer gradually carbonizes to Cr_3C_2 , which progressively spalls and detaches, diminishing the anti-carburization effect of Cr_2O_3 to disappear.

ance. The subsurface SiO_2 layer remains unchanged due to its excellent thermodynamic stability, but its discontinuity resulting from low Si activity allows some carbon penetration through oxide scale gaps.

3. When the composite oxide scale is removed or its anti-carburization capability severely degrades after sufficient carburization time, the tube material undergoes dramatic microstructural changes: interdendritic carbides severely coalesce and coarsen, transforming in situ from M_{23}C_6 to M_7C_3 , while vermicular γ -phase precipitates within carbides resembling a divorced eutectoid structure. At 1080 °C and high carbon activity, the γ -phase formed during long-term evolution transforms back to NbC.
4. Severe Cr depletion and C enrichment in the γ matrix around carbides cause carbon supersaturation in carbides. With increasing carbon activity nearer the surface, metal dusting characterized by massive graphite precipitation occurs within approximately 0.5 mm depth. Severe carbide coalescence/coarsening and metal dusting cause serious microstructural degradation, macro-crack formation, and tube wall thinning.

References

- [1] Khodamorad S H, Haghshenas F D, Rezaie H, Sadeghipour A. Eng Fail Anal, 2012; 21: 1
- [2] Al-Meshari A, Al-Rabie M, Al-Dajane M. J Fail Anal Prev, 2013; 13: 282
- [3] Tari V, Najafizadeh A, Aghaei M, Mazloumi M. J Fail Anal Prev, 2009; 9: 316
- [4] Zhang J, Young D J. Oxid Met, 2008; 70(3-4): 189
- [5] Chauhan A, Anwar M, Montero K, White H, Si W. J Phase Equilib Diff, 2006; 27: 684
- [6] Mitchell D, Young D, Kleemann W. Mater Corros, 1998; 49: 231
- [7] Ramanarayanan T, Petkovic R, Mumford J, Ozekcin A. Mater Corros, 1998; 49: 226
- [8] Rahmel A, Grabke H, Steinkusch W. Mater Corros, 1998; 49: 221
- [9] Oquab D, Xu N, Monceau D, Young D. Corros Sci, 2010; 52: 255
- [10] Kaya A A. Mater Charact, 2002; 49: 23
- [11] Grabke H, Wolf I. Mater Sci Eng, 1987; A87: 23
- [12] Giggins C, Pettit F. Oxid Met, 1980; 14: 363
- [13] Borjali S, Allahkaram S R, Khosravi H. Mater Des, 2012; 34: 65
- [14] Mostafaei M, Shamanian M, Purmohamad H, Amini M, Saatchi A. Eng Fail Anal, 2011; 18: 164
- [15] Paz J N, Grabke H. Oxid Met, 1993; 39: 437
- [16] Petkovic-Luton R, Ramanarayanan T. Oxid Met, 1990; 34: 381
- [17] Hermse C, Asteman H, IJzerman R, Jakobi D. Mater Corros, 2013; 64: 856
- [18] Sustaita-Torres I A, Haro-Rodríguez S, Guerrero-Mata M P, de la Garza M, Valdés E, Deschaux-Beaume F, Colás R. Mater Chem Phys, 2012; 133: 1018
- [19] Kunzru D. In: Sara R K, Ray S, Maity B R, Ganguly S, Bhattacharyya D, Chakraborty S L eds., Petroleum Refining and Petrochemical Based Industries

- in Eastern India, New Delhi: Allied Publishers Ltd., 2000: 14
- [20] Kaya A, Krauklis P, Young D. Mater Charact, 2002; 49: 11
 - [21] Bennett M, Price J. J Mater Sci, 1981; 16: 170
 - [22] Song R K, Zhang M C, Dong J X, Du C Y. Adv Mater Res, 2014; 834: 390
 - [23] Ryzhov N, Smirnov A, Fakhurtdinov R, Mulyakaev L, Gromov V. Met Sci Heat Treat, 2004; 46: 230
 - [24] Ramanarayanan T, Srolovitz D. J Electrochem Soc, 1985; 132:
 - [25] Wagner C. J Electrochem Soc, 1952; 99(10): 369

Note: Figure translations are in progress. See original paper for figures.

Source: ChinaXiv –Machine translation. Verify with original.